IEEE Photonics Journal
An IEEE Photonics Society Publication

Open Access

Nonlinear Bound States in the Continuum of Etchless Lithium Niobate Metasurfaces

Volume 12, Number 5, October 2020

Qiyu Yang
Yan Liu
Xuetao Gan
Cizhe Fang
Genquan Han, *Member, IEEE*
Yue Hao, *Senior Member, IEEE*

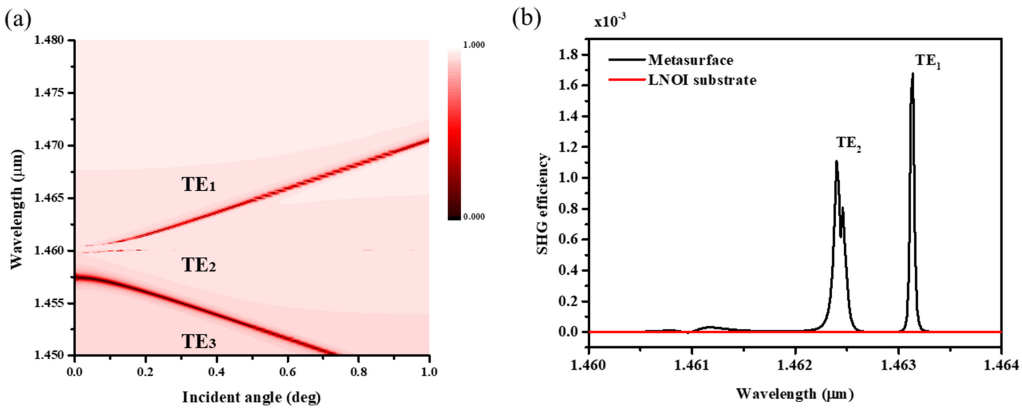

DOI: 10.1109/JPHOT.2020.3024789

Nonlinear Bound States in the Continuum of Etchless Lithium Niobate Metasurfaces

Qiyu Yang,[1] Yan Liu,[1] Xuetao Gan,[2] Cizhe Fang,[1] Genquan Han,[1] *Member, IEEE*, and Yue Hao,[1] *Senior Member, IEEE*

[1]Wide Bandgap Semiconductor Technology Disciplines State Key Laboratory, School of Microelectronics, Xidian University, Xi'an 710071, China
[2]MOE Key Laboratory of Material Physics and Chemistry under Extraordinary Conditions, and Shaanxi Key Laboratory of Optical Information Technology, School of Physical Science and Technology, Northwestern Polytechnical University, Xi'an 710129, China

DOI:10.1109/JPHOT.2020.3024789

Manuscript received August 17, 2020; revised September 5, 2020; accepted September 11, 2020. Date of publication September 18, 2020; date of current version October 8, 2020. This work was supported in part by the National Key Research and Development Project under Grants 2018YFB2200500 and 2018YFB2202800, and in part by the National Natural Science Foundation of China under Grants 61534004, 91964202, 61874081, and 61851406. Corresponding author: Yan Liu (e-mail: xdliuyan@xidian.edu.cn).

Abstract: Optical bound states in the continuum (BICs) have recently been studied in a wide range of material systems, where light is perfectly confined in the continuous spectrum of radiating modes. In this paper, we reported periodic nonlinear metasurfaces on the etchless $LiNbO_3$ platform, realizing the enhancement of second-order generation (SHG). All-dielectric heterogeneous metasurfaces are constructed by patterning a low-refractive-index polymer on a high refractive-index $LiNbO_3$ film without etching. Due to BICs, light is localized in the $LiNbO_3$ film where the excellent optical second-order nonlinearity is exploited. We demonstrated that with normal incident waves, symmetry-protected BICs are formed at near-infrared wavelength showing a vanishing linewidth in the transmission spectrum. In addition, to manifest the invisible BICs to detectable supercavity resonances at normal incidence, asymmetry is introduced into the system, degrading the symmetry-protected BICs to sharp resonances with a high Q factor. Furthermore, the second harmonic generation (SHG) of the etchless lithium niobate metasurface is studied, predicting that the SHG efficiency can exceed 10^{-3} with 30 MW/cm^2 of the pump intensity. The proposed strategy without facing the fabrication challenge of etching single-crystal $LiNbO_3$ film opens a new avenue for the utilization of BIC in nonlinear optics of all-dielectric heterogeneous metasurfaces.

Index Terms: Bound states in the continuum, All-dielectric metasurface Second-harmonic generation.

1. Introduction

The electromagnetic metasurface is a kind of special quasi-2D meta-material consisting of ultrathin subwavelength structures with different shapes and sizes. It has recently aroused great research attention in the field of optics [1]–[6]. Through structural geometries variation, metasurfaces can modulate the polarization, phase, and amplitude of the propagating waves [7]–[11]. Strongly interacting with electromagnetic waves, metasurfaces can offer a completely new route for nonlinear optics [12], [13]. As common nonlinear optical effects, nonlinear wave mixing such as second-harmonic generation and third-harmonic generation are generally realized based on the conventional phase

matching concept in bulk structures. With strong light-matter interaction, ultrathin metasurfaces are capable of replacing conventional macroscopic structures and realizing high wavelength conversion efficiencies in the meantime [13]. The study of nonlinear effects within ultrathin metasurfaces was firstly investigated in the plasmonic metasurfaces constructed by split-ring metal resonators [14], [15]. However, metals show significant Ohmic loss beyond the microwave frequencies, resulting in relatively low Q factors in the conventional plasmonic metasurfaces, which limits their application in various functional nanoscale devices [16]–[18]. To bypass this restriction, all-dielectric platforms with the promise to offer low-loss meta-optics and photonics attracts growing interest in recent years [18], [19]. Lithium Niobate ($LiNbO_3$) is a kind of transparent dielectric material with an insignificant absorption coefficient of 10^{-5} in visible to near-IR frequency range [20]. Moreover, The hexagonal non-centrosymmetric crystal structure of $LiNbO_3$ [21] facilitates strong nonlinear effects such as electro-optical effect, piezoelectricity, and large second-order nonlinear coefficient ($d_{33} = 25$ pm/V), which has the potential of enabling ultra-fast optical switches, SAW (Surface Acoustic Wave) transducers, and wavelength conversion [22]. Owing to the nonliearlity of $LiNbO_3$ crystal, $LiNbO_3$ metasurfaces and nanostructures has been studied in the nonliear optics, where second-harmonic generation is emphasized [23]–[26]. However, $LiNbO_3$ is perceived as a difficult-to-etch material. The available etching methods such as Ar milling and mixed fluorine and argon plasma etching still face the challenges of realizing steep sidewall, large etch depth, and low losses [27]–[29]. To construct nonlinear $LiNbO_3$ metasurfaces without etching, we employ a recently emphasized concept of optical bound states in the continuum (BICs) enabling a convenient approach to realize effective light localization and to enhance second-harmonic generation in $LiNbO_3$ metasurfaces.

Bound states in the continuum (BICs) was originally predicted by von Neumann and Wigner in 1929 [30] with mathematically designing a quantum potential to trap an electron in the states where energy would normally allow the coupling to radiating waves. As a wave phenomenon can be interpreted by destructive interference, the concept of BICs has been extended to acoustics [31]–[33], photonics [34]–[36], and electronics [37]–[41]. Recently, the advancement of nanofabrication technologies has enabled the fast development of BICs in photonic nanostructures, promoting practical applications in a wide range of areas such as sensors [42]–[44], lasers [45], and filters [46]. Because the BIC mechanism promises tight confinement of photons in a high-refractive-index material surrounded by a low-refractive-index environment, the reported optical BICs are mostly realized in the conventional structures, such as passive photonic crystal slabs [47], waveguide arrays [48], nanoparticles [49], and anisotropic dielectric layers [50]. However, it has also been reported that the optical BICs can exist in a high-refractive-index substrate with low-refractive-index waveguides atop by precisely tuning the dimensional parameters to achieve destructive interference between the leaky channels to the substrate [51]–[53], which can be explained by Friedrich-Wintgen BICs [54].

As is recently reported, BICs have been employed in silicon-based resonant metasurfaces to enhance nonlinear optical effects, such as third-harmonic generation [55], [56]. However, due to centrosymmetry of Si crystal, Si shows no second order nonlinearity without strain or applied electric field. In this paper, we designed all-dielectric nonlinear metasurfaces with low-refractive-index polymer cuboid nanopillars on the $LiNbO_3$-on-insulator (LNOI) substrate based on the mechanism of bound states in the continuum. The existence of the symmetry protected BIC modes in the designed metasurfaces are demonstrated by employing the finite element method (FEM). The BIC mode exhibits magnetic dipole (MD) resonance in the near-IR wavelength range. Furthermore, by introducing in-plane symmetry breaking to highly symmetric polymer nanopillars, the true symmetry protected BICs transformed into quasi-BIC modes with a relatively high Q factor (up to 10^5). Finally, we illustrated the enhanced second-harmonic generation resulting from the strong field confinement in the L-shaped metasurfaces utilizing the high Q quasi-BIC modes. Our results show that based on the mechanism of BIC (or quasi-BIC) resonance, we can confine light in the single-crystal $LiNbO_3$ film and thus enhance second-harmonic generation in the heterogeneous metasurfaces.

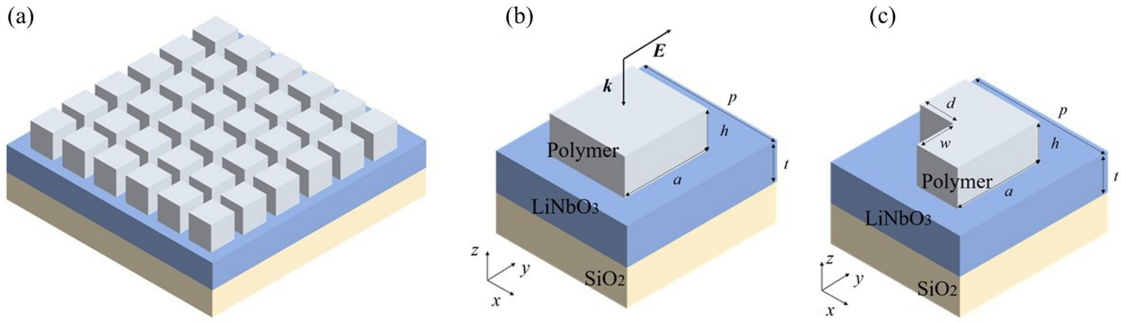

Fig. 1. (a) 3D schematic of the designed etchless $LiNbO_3$ metasurfaces. (b) Schematic diagram of a single unit with in-plane symmetry. (c) Schematic diagram of a single unit with L-shaped nanopillar.

2. Device Structure

We proposed a design of the periodic metasurface with in-plane symmetry to support symmetry-protected BIC, as shown in Fig. 1(a). In the finite element method (FEM) simulation, a normal incident plane wave with a wave vector, k is parallel to the z-axis, and the electric field, E, polarized along the y-axis, as shown in Fig. 1(b). To simulate a semi-infinite situation of a periodic structure, a single unit cell is calculated in x-y planes with periodic boundary conditions while perfectly matched layers are used along the z-axis. The refractive index of the polymer is set as 1.5, and because the dispersion of the refractive index of $LiNbO_3$ changes slightly in visible to the near-IR range, whose refractive index is set as 2.14. The height of polymer nanopillar, the side length of polymer nanopillar, the period of the unit cell, the thickness of $LiNbO_3$ crystal, the length of the defect, and the width of the defect are denoted by h, a, p, t, d, and w respectively. To construct a BIC in the near-IR frequency range, the geometrical parameters of periodic metasurfaces with in-plane symmetry is set as $h = 400$ nm, $a = 520$ nm, $p = 780$ nm, $t = 400$ nm, and the fused silica is cut off as a perfectly matched layer indicating an infinite thickness to emulate a $LiNbO_3$-on-insulator wafer. To investigate the properties of BIC (or quasi-BIC) mode at Γ point, we introduced in-plane symmetry-breaking perturbations to transform the ideal symmetry-protected BIC into supercavity (quasi-BIC) mode accompanied by high Q factor resonances [57]. As shown in Fig. 1(c), without changing other geometrical parameters, we removed part of the nanopillars with in-plane symmetry forming an L-shaped metasurface with the length of the defect $d = 195$ nm, the width of the defect $w = 260$ nm.

3. Results and Discussion

In this section, we first demonstrate the spectral features of the metasurfaces on a high-refractive-index $LiNbO_3$ film. Firstly we overview the band structure of the periodic metasurfaces. With the Bloch wave vector changes along $\vec{k} = (k_x, 0, 0)$, the band structure is calculated in COMSOL Multiphysics. The eigenfrequency is represented as a complex frequency f, which enables the calculation of radiative quality factor as

$$Q = \frac{\mathrm{Re}(f)}{2\mathrm{Im}(f)} \tag{1}$$

The resonance frequency and radiation losses are given by the real and imaginary parts of the complex eigenfrequency f respectively. According to the occurrence order in the spectrum, the lowest two TE modes TE_1, TE_2 and TE_3, and the lowest TM mode TM_1 are exhibited in the band diagram, as shown in Fig. 2(a). The Q factor of TE_1 mode and TE_2 mode is calculated with equation (1) in Fig. 2(b). It can be seen from Fig. 2(b), the infinite Q factor of TE_1 mode and TE_2 mode drop rapidly near Γ point, indicating at normal incidence, the modes become true

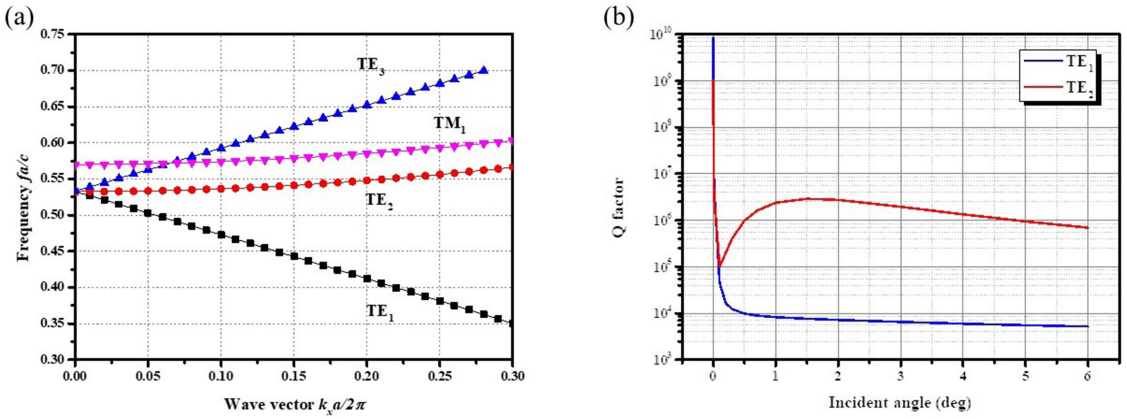

Fig. 2. (a) The band diagram of periodic metasurface with in-plane symmetry. (b) The dependence of the Q factor on the incident angle for TE_1 mode and TE_2 mode.

BIC modes with infinite Q factor (more than 10^9). These BIC at Γ point are symmetry-protected BICs generating from the mirror and rotational symmetry incompatibility between the bound mode and the radiative modes [47]. Symmetry-protected BIC can exist in various optical structures [35], [48], since symmetry-protected BIC is formed by the complete decoupling of modes of different symmetry classes.

In this structure, we focus on the symmetry-protected BIC excited by TE_1 mode. This symmetry-protected BIC is robust against the dimensional changes while preserving the spatial symmetry (i.e. variation of period *p* and side length *a*) [57]. As the angular-resolved transmission spectra shown in Fig. 3(a) and Fig. 3(b), it can be seen that the BIC excited by TE_1 mode is formed at 1461.5 nm at Γ point. The TE_1 mode shows vanishing resonance linewidth as the incident angle decreases to zero, which is consistent with the infinite Q factor of TE_1 at $\vec{k} = 0$ in Fig. 2(b). Evolution of transmission spectra vs incident angle shown in Fig. 3(c) demonstrates the noticeable and sudden appearance of narrow resonances when moving away from the symmetry-protected BICs in the *k* space. In the vicinity of the symmetry-protected BIC, the Q factor degrades quickly with the increase of the incident angle θ. When θ increases from 0° to 1°, the corresponding Q factor decreases from more than 10^9 to about 10^4, as shown in Fig. 2(b), which can be called "near-BIC" region. The near-BIC region with a relatively high Q factor is obtained by continuously varying the parameters (including wave vector and geometrical parameters) away from the specific BIC value. At the BIC point, the true BIC mode has no leakage and is decoupled from any radiation channels, resulting in a completely dark mode, which disappears in the transmission spectrum, as shown in Fig. 3(c) when $\theta = 0^o$. In the near-BIC region, the high Q factor can be explained by the resonance reaction theory [58], [59]. In the near-BIC region, a bound state can exist in the radiation continuum when the mode couples to the radiation channels. When the Hamiltonian producing this bound state differs slightly from the actual Hamiltonian, a sharp resonance occurs in scattering and reaction sections, which results in a comparably high Q factor. The Q factor decreases fast in the near-BIC region, showing an exponential decay with the varying parameter [60]. To deeply understand the physics of the near-BIC region, the electric field and magnetic field profile of BIC mode at $\theta = 0^o$ and $\theta = 0.1^o$ are shown in Fig. 3(d) and Fig. 3(e) respectively. The field profile indicates a *z*-directed magnetic dipole (MD) resonance feature, exhibiting an in-plane circular current behavior. The electric field manifests the BIC mode as a TE-like mode at Γ point. Away from the polymer nanopillar, the magnetic field has the opposite directions in the $LiNbO_3$ film, indicating the magnetic dipole resonance is not confined only under the polymer nanopillar. Besides, in the near-BIC region (e.g., $\theta = 0.1^o$), the MD resonance shows a trend of leakage along *y*-axis, as shown in Fig. 3(e), but still dominants the resonance.

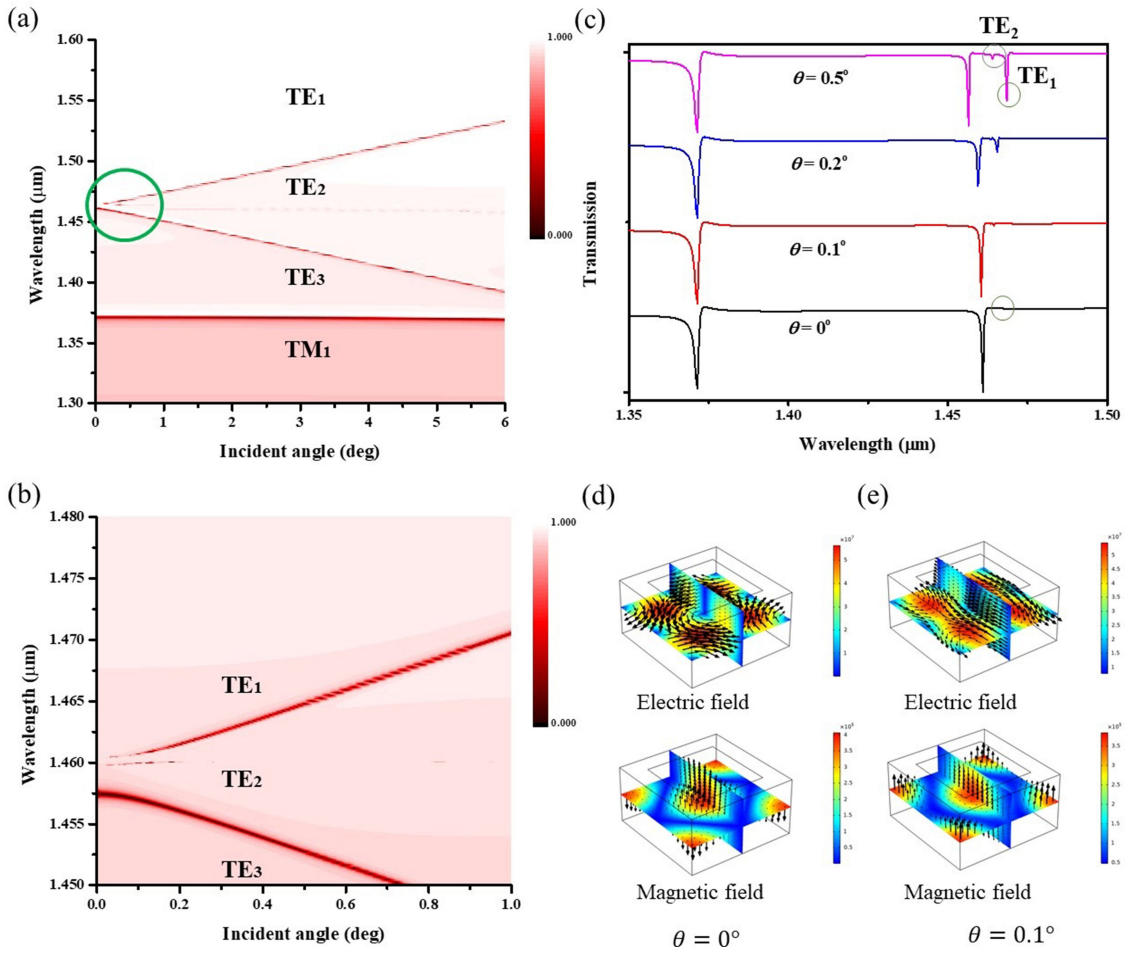

Fig. 3. (a) Angular-resolved transmission spectrum calculated for the periodic metasurface with in-plane symmetry. (b) Angular-resolved transmission spectrum when incident angle is smaller than 1°. (c) Evolution of transmission spectra vs incident angle from 0° to 0.5°. (d) Electric and magnetic field distribution in the $LiNbO_3$ film under the nanopillars at $\theta = 0^o$. (e) Electric and magnetic field distribution in the $LiNbO_3$ film under the nanopillars at $\theta = 0.1^o$.

By removing part of the nanocube to introduce in-plane symmetry perturbation, the L-shaped nanopillar is studied as follows. Fig. 4(a) shows the dependence of Q factor on the incident angle for TE_1 mode in L-shaped metasurfaces ($d = 195$ nm, $w = 260$ nm). The maximum Q factor is obtained at normal incidence, showing a high Q factor of more than 13000. With the incident angle increases, the Q factor declines slowly comparing to the true BIC case. The field distribution of E_x and H_z at Γ point are shown in Fig. 4(b) and Fig. 4(c) for symmetric nanocube metasurfaces and L-shaped nanopillar metasurfaces respectively. The magnetic field presents *z*-directed magnetic dipole (MD) features in the $LiNbO_3$ film, and the magnetic dipoles have opposite directions under and away from the nanopillar. In the vertical section of E_x, which can be seen that the intensity of the electric field decreases away from the $LiNbO_3$ film, indicating this BIC mode does not radiate in the vertical direction along the *z*-axis. When the symmetry perturbation is introduced, the electric field extends out of $LiNbO_3$ film, and the intensity of light localized in the $LiNbO_3$ film is reduced. As can be seen in Fig. 4(b) and Fig. 4(c), when the symmetry perturbation is introduced, the magnetic field extends to the area with no polymer atop while the MD resonance is still supporting the resonance. To illustrate the influence of the defect size on the Q factor, the size of the defect is interpreted as asymmetry parameter α, defined as the ratio of the removed part to the area of the

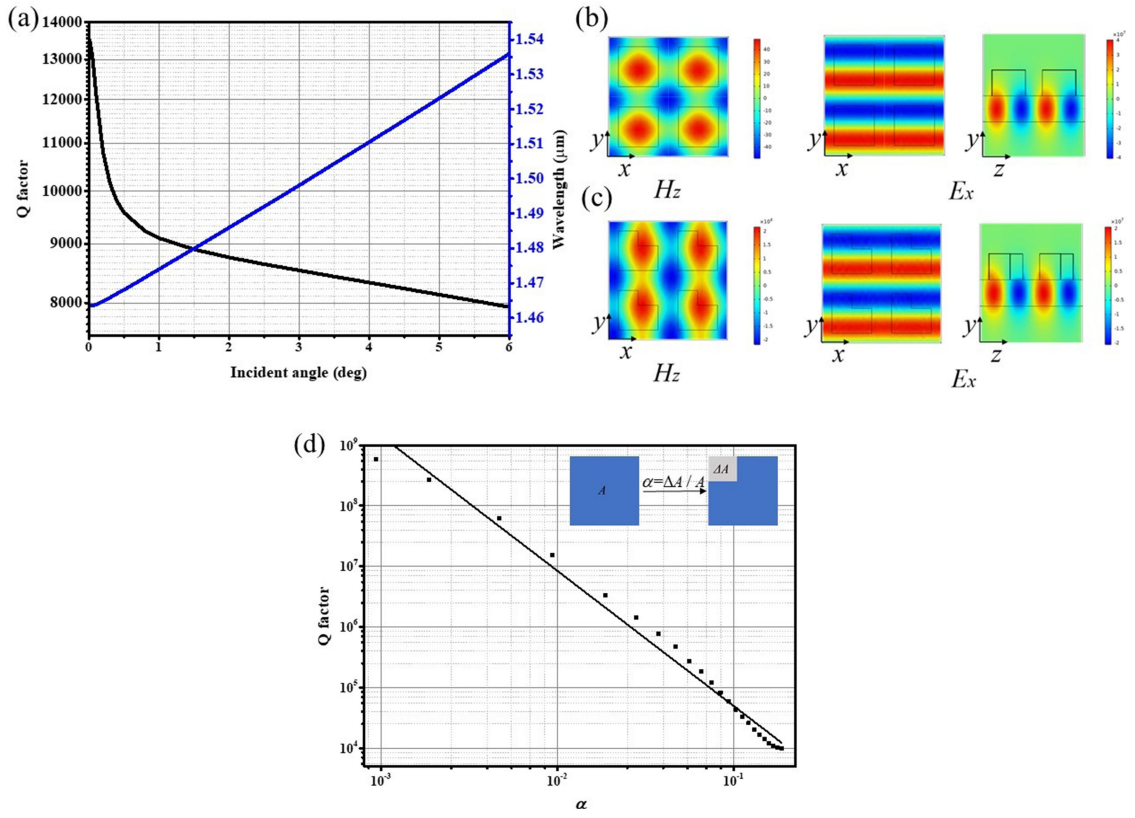

Fig. 4. (a) The dependence of Q factor on the incident angle for TE_1 mode in L-shaped metasurfaces. (b) H_z and E_x distribution corresponding to the metasurfaces with in-plane symmetry at the *x-y* cross-section in the middle of the $LiNbO_3$ film, E_x distribution at the *y-z* cross-section. (c) H_z and E_x distribution corresponding to the L-shaped metasurfaces at the *x-y* cross-section in the middle of the $LiNbO_3$ film, E_x distribution at the *y-z* cross-section. (d) Modeled Q factor of TE_1 as a function of the asymmetry parameter, α. Inset: definition of the asymmetry parameter.

polymer. We fixed the length *d* of the defect to be 195 nm and varied the width of the defect *w* to tune the asymmetry parameter. As obtained in Fig. 4(d), the Q factor of the quasi-BIC mode scales as inverse square law with the asymmetry parameter of the polymer nanopillars [61].

As is mentioned above, true BICs perfectly confine light in the metasurface and do not radiate. Introducing symmetry-breaking tunes the true symmetry-protected BIC to quasi-BIC, obtaining a high Q factor mode at normal incidence. For the asymmetry L-shaped metasurface, we simulated linear transmission, which demonstrates a sharp dip at the quasi-BIC wavelength (see Fig. 4(a)). Moreover, we calculated the second-harmonic generation related to the quasi-BIC resonance. Since $LiNbO_3$ is a non-centrosymmetric material with large second-order nonlinear susceptibility, $LiNbO_3$ single-crystal film itself has a great potential in second-order nonlinear optics. To demonstrate the potential of etchless $LiNbO_3$ metasurfaces for second-harmonic generation, the second-order nonlinear polarization is set as a source in FEM. The SHG efficiency is defined as

$$\eta_{SHG} = \frac{\int_A \overrightarrow{S_{SH}} \cdot \hat{n} da}{I_0 \times p^2} \tag{2}$$

where $\overrightarrow{S_{SH}}$ is the Energy flux density vector of the second-harmonic field, *A* is the integration surface enclosing the LiNbO3 unit cell $\hat{n}$ is the unit vector normal to surface *A*, and I_0 is the fundamental wave intensity ($I_0 = 30$ MW/cm^2 in the simulations). The normalized transmission spectrum of an asymmetry metasurface with $w = 156$ nm, $d = 195$ nm is shown in Fig. 5(a). The calculated

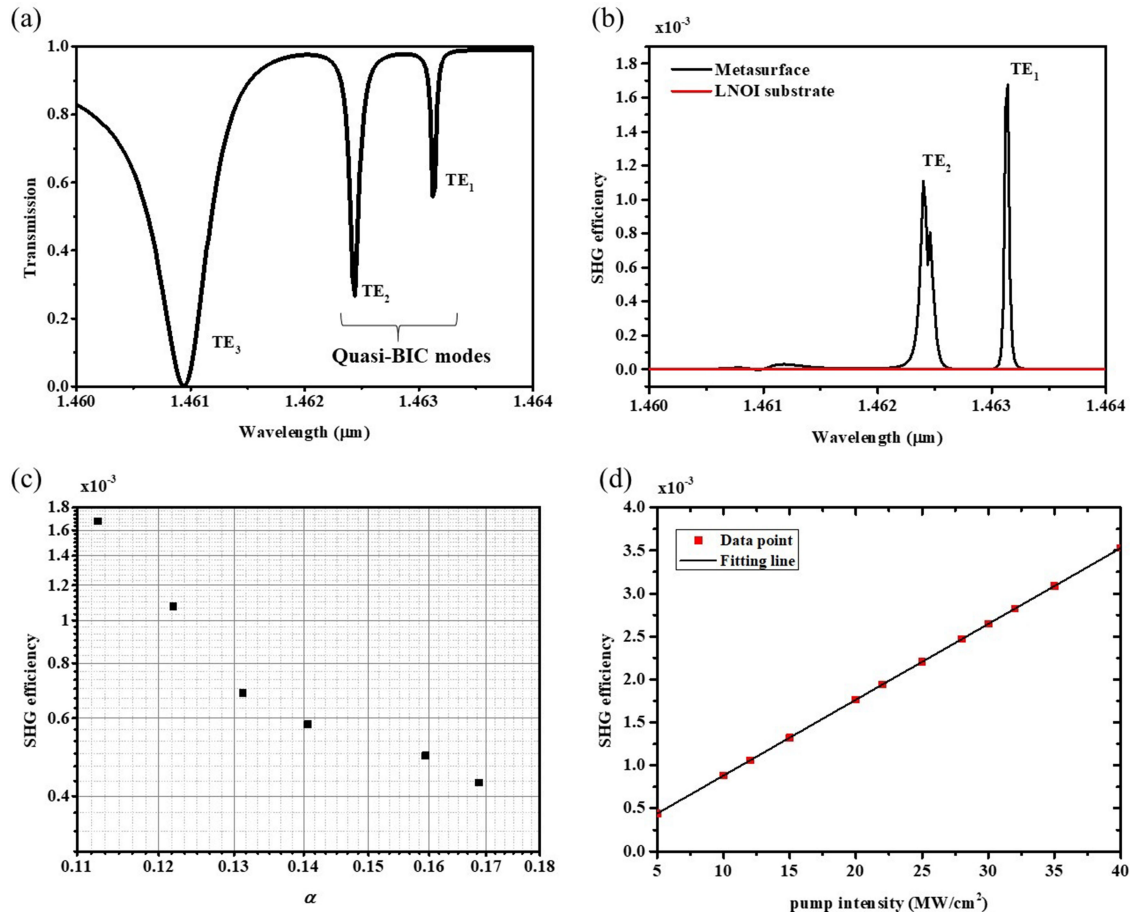

Fig. 5. (a) The normalized transmission spectrum of L-shaped metasurface with w = 156 nm, d = 195 nm and pump intensity $I_0 = 30$ MW/cm^2. (b) SHG efficiency as a function of pump wavelength for an L-shaped metasurface. (c) Maximum SHG efficiency as a function of the asymmetry parameter α of the L-shaped nanopillars. (d) Dependence of SHG efficiency on the fundamental wave pump intensity

SHG efficiency for the LNOI substrate without polymer nanopillar and the asymmetry metasurface mentioned above are shown in Fig. 5(b). In the calculation, we used the dominating nonlinear coeffcient $d_{33} = 25$ pm/V as reported for z-cut $LiNbO_3$ in [57]. As Fig. 5(b) shows, the peaks of SHG efficiency are obtained for pump wavelengths of $\lambda = 1462.5$ nm and $\lambda = 1463$ nm, which are exactly the quasi-BIC resonance wavelengths indicated in Fig. 5(a). The maximum SHG efficiency corresponds to the quasi-BIC excited by TE_1 mode at $\lambda = 1463$ nm. Besides, the SHG efficiency of the LNOI substrate is insignificant comparing to the metasurface, which confirms the enhancement is generated from the designed metasurface. Fig. 5(c) shows the maximum SHG efficiency as a function of the asymmetry parameter α of the L-shaped polymer nanopillar. With α decreasing, the maximum SHG efficiency increases. More specifically, the SHG efficiency scales as an inverse square law with the asymmetry parameter, similar to the way that the Q factor scales with the asymmetry parameter. It can be explained by the definition of second-order polarization intensity $P^{(2)} = \varepsilon_0 \chi^{(2)} E_1 E_1$, where E_1 is the electric field intensity of the incident fundamental wave. Based on the BIC mechanism, the quasi-BIC in the $LiNbO_3$ film confines light in the layer to obtain large electric field intensity and the high Q factor. The large field intensity gives rise to the second-order polarization intensity, which affects the SHG efficiency to show the same trend as the Q factor and the field intensity with the asymmetry parameter varying. As shown in Fig. 5(d), the SHG efficiency

is proportional to the pump intensity, which means a quadratic relation between SH intensity and fundamental wave intensity, showing good agreement with the nature of second-order generation process.

4. Conclusion

In this work, we demonstrated etchless heterogeneous lithium niobate metasurfaces by patterning low-refractive-index polymer nanopillars on high-refractive-index $LiNbO_3$ film. A symmetry-protected BIC with an infinite Q factor is formed when the metasurfaces remain in-plane symmetry. By removing partial material of the polymer nanopillars, a sharp resonance caused by quasi-BIC mode is achieved. Besides, utilizing these quasi-BIC modes, second harmonic generation in the $LiNbO_3$ film is enhanced at the resonance frequency, achieving SHG efficiency of more than 10^{-3}. The relationship between the asymmetry parameter and SHG efficiency is also investigated, showing a decreasing SHG efficiency as the asymmetry parameter increasing. The results provided by this work opens a new avenue for manipulating symmetry protected BIC and utilizing functional single-crystal materials in nonlinear optics with convenient fabrication processes. We believe this approach has a huge potential for applications such as molecular sensing and lasering.

References

[1] N. Yu and F. Capasso, "Flat optics with designer metasurfaces," *Nat. Mater.*, vol. 13, no. 2, pp. 139–150, 2014.
[2] N. Yu *et al.*, "Light propagation with phase discontinuities: Generalized laws of reflection and refraction," *Science*, vol. 334, no. 6054, p. 333, 2011.
[3] M. Khorasaninejad, W. T. Chen, R. C. Devlin, J. Oh, A. Y. Zhu, and F. Capasso, "Metalenses at visible wavelengths: Diffraction-limited focusing and subwavelength resolution imaging," *Science*, vol. 352, no. 6290, pp. 1190–1194, 2016.
[4] D. Lin, P. Fan, E. Hasman, and M. L. Brongersma, "Dielectric gradient metasurface optical elements," *Science*, vol. 345, no. 6194, pp. 298–302, 2014.
[5] X. Ni, N. K. Emani, A. V. Kildishev, A. Boltasseva, and V. M. Shalaev, "Broadband light bending with plasmonic nanoantennas," *Science*, vol. 335, no. 6067, pp. 427–427, 2012.
[6] S. Sun *et al.*, "High-efficiency broadband anomalous reflection by gradient meta-surfaces," *Nano Lett.*, vol. 12, no. 12, pp. 6223–6229, 2012.
[7] N. I. Zheludev and Y. S. Kivshar, "From metamaterials to metadevices," *Nat. Mater.*, vol. 11, no. 11, pp. 917–924, 2012.
[8] A. Zhan, S. Colburn, C. M. Dodson, and A. Majumdar, "Metasurface freeform nanophotonics," *Sci. Rep.*, vol. 7, no. 1, 2017, Art. no. 1673.
[9] W. T. Hsieh, P. C. Wu, J. B. Khurgin, D. P. Tsai, N. Liu, and G. Sun, "Comparative analysis of metals and alternative infrared plasmonic materials," *ACS Photon.*, vol. 5, no. 7, pp. 2541–2548, 2017.
[10] M. Pu *et al.*, "Catenary optics for achromatic generation of perfect optical angular momentum," *Sci. Adv.*, vol. 1, no. 9, 2015, Art. no. e1500396.
[11] Y. F. Yu, A. Y. Zhu, R. Paniaguadominguez, Y. H. Fu, B. S. Lukyanchuk, and A. I. Kuznetsov, "High-transmission dielectric metasurface with 2π phase control at visible wavelengths," *Laser Photon. Rev.*, vol. 9, no. 4, pp. 412–418, 2015.
[12] G. Li, S. Zhang, and T. Zentgraf, "Nonlinear photonic metasurfaces," *Nature Rev. Mater.*, vol. 2, 2012, Art. no. 17010.
[13] A. Krasnok, M. Tymchenko, and A. Alu, "Nonlinear metasurfaces: A paradigm shift in nonlinear optics," *Mater. Today*, vol. 21, pp. 8–21, 2018.
[14] M. W. Klein, C. Enkrich, M. Wegener, and S. Linden, "Second harmonic generation from magnetic metamaterials," *Science*, vol. 313, 502–504, 2006.
[15] A. Boltasseva and H. A. Atwater, "Low-loss plasmonic metamaterials," *Science*, vol. 331, no. 6015, pp. 290–291, 2011.
[16] F. Dreisow *et al.*, "Adiabatic transfer of light via a continuum in optical waveguides," *Opt. Lett.*, vol. 34, no. 16, pp. 2405–2407, 2009.
[17] J. M. Foley, S. Young, and J. D. Phillips, "Symmetry-protected mode coupling near normal incidence for narrow-band transmission filtering in a dielectric grating," *Phys. Rev. B*, vol. 89, no. 16, 2014, Art. no. 165111.
[18] S. Kruk and Y. Kivshar, "Functional meta-optics and nanophotonics governed by Mie resonances," *ACS Photon.*, vol. 4, no. 11, 2017, Art. no. 2638.
[19] A. Cardin, K. Fan, and W. J. Padilla, "Role of loss in all-dielectric metasurfaces," *Opt. Express*, vol. 26, no. 13, pp. 17669–17679, 2018.
[20] E. D. Palik, "Lithium niobate (LiNbO3)." In *Handbook of Optical Constants of Solids I*. San Diego, CA, USA: Academic Press, 1997, pp. 695–702.
[21] R. S. Weis and T. K. Gaylord, "Lithium niobate: Summary of physical properties and crystal structure," *Appl. Phys. A: Solids Surf.*, vol. 37, pp. 191−203, 1985.
[22] I. Shoji *et al.*, "Absolute scale of second-order nonlinear-optical coefficients," *J. Opt. Soc. Am. B*, vol. 14, 1997, Art. no. 2268.

[23] F. Timpu *et al.*, "Lithium niobate nanocubes as linear and nonlinear ultraviolet mie resonators," *ACS Photon.*, vol. 6, no. 2, pp. 545–552, 2019.
[24] Y. Li *et al.*, "Optical anapole mode in nanostructured lithium niobite," *Nanophotonics*, vol. 9, pp. 3575–3585, 2020.
[25] B. Gao *et al.*, "Lithium niobate metasurfaces," *Laser Photon. Rev.*, vol. 13, 2019, Art. no. 1800312.
[26] L. Carletti *et al.*, "Second harmonic generation in monolithic lithium niobate metasurfaces," *Opt. Express*, vol. 27, Art. no. 33391–33398, 2019.
[27] I. Krasnokutska *et al.*, "Ultra-low loss photonic circuits in Lithium niobate on insulator," *Opt. Express*, vol. 26, no. 2, pp. 897–904, 2018.
[28] H. Hu *et al.*, "Lithium niobate photonic wires," *Opt. Express*, vol. 17, no. 26, pp. 24261–24268, 2009.
[29] M. Zhang *et al.*, "Monolithic ultra-high-Q lithium niobate microring resonator," *Optica*, vol. 4, no. 12, pp. 1536–1537, 2017.
[30] J. Von Neumann and Wigner, "About strange discrete eigen values," (in German), *Phys. Z.*, vol. 30, pp. 465–467, 1929.
[31] R. Parker, "Resonance effects in wake shedding from parallel plates: Some experimental observations," *J. Sound Vib.*, vol. 4, no. 1, pp. 62–72, 1966.
[32] R. Parker, "Resonance effects in wake shedding from parallel plates: Calculation of resonant frequencies," *J. Sound Vib.*, vol. 5, no. 2, pp. 330–343, 1967.
[33] A. A. Lyapina *et al.*, "Bound states in the continuum in open acoustic resonators," *J. Fluid Mech.*, vol. 780, pp. 370–387, 2015.
[34] M. R. Watts, S. G. Johnson, H. A., and Haus, J. D. Joannopoulos, "Electromagnetic cavity with arbitrary Q and small modal volume without a complete photonic bandgap," *Opt. Lett.*, vol. 27, pp. 1785–1787, 2002.
[35] D. C. Marinica, A. G. Borisov, and S. V. Shabanov, "Bound states in the continuum in photonics," *Phys. Rev. Lett.*, vol. 100, 2008, Art. no. 183902.
[36] M. I. Molina, A. E. Miroshnichenko, and Y. S. Kivshar, "Surface bound states in the continuum," *Phys. Rev. Lett.*, vol. 108, 2012, Art. no. 070401.
[37] A. Albo, D. Fekete, and G. Bahir, "Electronic bound states in the continuum above (Ga, In)(As, N)/(Al, Ga) As quantum wells," *Phys. Rev. B*, vol. 85, 2012, Art. no. 115307.
[38] C. Álvarez *et al.*, "Impact of electron–vibron interaction on the bound states in the continuum," *Phys. Lett. A*, vol. 379, pp. 1062–1066, 2015.
[39] J. X. Yan and H. H. Fu, "Bound states in the continuum and Fano antiresonance in electronic transport through a four-quantum-dot system," *Phys. B: Condens. Matter*, vol. 410, pp. 197–200, 2013.
[40] W. J. Gong, Y. Han, and G. Z. Wei, "Antiresonance and bound states in the continuum in electron transport through parallel-coupled quantum-dot structures," *J. Phys.: Condens. Matter.*, vol. 21, 2009, Art. no. 175801.
[41] L. De Guevara, M. L., and P. A. Orellana, "Electronic transport through a parallel-coupled triple quantum dot molecule: Fano resonances and bound states in the continuum," *Phys. Rev. B*, vol. 73, 2006, Art. no. 205303.
[42] Y. H. Liu, W. D. Zhou, and Y. Z. Sun, "Optical refractive index sensing based on high-Q bound states in the continuum in free-space coupled photonic crystal slabs," *Sensors*, vol. 17, 2017, Art. no. 1861.
[43] B. Zhen *et al.*, "Enabling enhanced emission and low-threshold lasing of organic molecules using special Fano resonances of macroscopic photonic crystals," in *Proc. Natl Acad. Sci. USA*, vol. 110, 13711–13716, 2013.
[44] Z. Fang *et al.*, "Germanium-tin alloys: Applications for optoelectronics in mid-infrared spectra," *Opto-Electron Adv.*, vol. 1, 2018, Art. no. 180004.
[45] A. Kodigala *et al.*, "Lasing action from photonic bound states in continuum," *Nature*, vol. 541, 196–199, 2017.
[46] J. M. Foley, S. M. Young, and J. D. Phillips, "Symmetry-protected mode coupling near normal incidence for narrow-band transmission filtering in a dielectric grating," *Phys. Rev. B*, vol. 89, 2014, Art. no. 165111.
[47] C. W. Hsu *et al.*, "Observation of trapped light within the radiation continuum," *Nature*, vol. 499, 188–191, 2013.
[48] Y. Plotnik *et al.*, "Experimental observation of optical bound states in the continuum," *Phys. Rev. Lett.*, vol. 107, 183901, 2011.
[49] M. V. Rybin *et al.*, "High-Q supercavity modes in subwavelength dielectric resonators," *Phys. Rev. Lett.*, vol. 119, 2017, Art. no. 243901.
[50] J. Gomis-Bresco, D. Artigas, and L. Torner, "Anisotropy-induced photonic bound states in the continuum," *Nat. Photon.*, vol. 11, pp. 232–236, 2017.
[51] C. - L. Zou *et al.*, "Guiding light through optical bound states in the continuum for ultrahigh-Q microresonators," *Laser Photon. Rev.*, vol. 9, no. 1, pp. 114–119, 2015.
[52] Z. Yu *et al.*, "High-dimensional communication on etchless lithium niobate platform with photonic bound states in the continuum," *Nat Commun.*, vol. 11, 2020, Art. no. 2602.
[53] Z. Yu and X. Sun, "Acousto-optic modulation of photonic bound state in the continuum," *Light Sci Appl.*, vol. 9, p. 1, 2020.
[54] C. W. Hsu, B. Zhen, A. D. Stone, J. D. Joannopoulos, and M. Soljacic, "Bound states in the continuum," *Nature Rev. Mater.*, vol. 1, no. 9, pp. 1–13, 2016.
[55] K. Koshelev, Y. Tang, K. Li, D.-Y. Choi, G. Li, and Y. Kivshar, "Nonlinear metasurfaces governed by bound states in the continuum," *ACS Photon.*, vol. 6, 2019, Art. no. 1639.
[56] Z. Liu *et al.*, "High-Q Quasi bound states in the continuum for nonlinear metasurfaces," *Phys. Rev. Lett.*, vol. 123, 2019, Art. no. 253901.
[57] M. Rybin and Y. Kivshar, "Supercavity lasing," *Nature*, vol. 541, 164–165, 2017.
[58] L. Fonda, "Resonance reactions and continuous channels," *Ann. Phys.*, vol. 12, no. 3, p. 476-484, 1961.
[59] L. Fonda, "Bound states embedded in the continuum and the formal theory of scattering," *Ann. Phys.*, vol. 22, p. 123, 1963.
[60] E. N. Bulgakov, "Nearly bound states in the radiation continuum in a circular array of dielectric rods," *Physical Rev. A*, vol. 97, no. 3, 2018.
[61] K. Koshelev, S. Lepeshov, M. Liu, A. Y Bogdanov, and Y. S. Kivshar, "Asymmetric metasurfaces with high-Q resonances governed by bound states in the continuum," *Phys. Rev. Lett*, vol. 121, no. 19, 2018, Art. no. 193903.